



Mixed-oxide $\text{Ti}_{1-x}\text{W}_x\text{O}_2$ as support for (photo)-electrochemical processes



S. Mokrane-Soualah^{a,b}, A.S. Gago^{a,1}, A. Habrioux^a, N. Alonso-Vante^{a,*}

^a IC2MP UMR-CNRS 7285, University of Poitiers, 4 rue Michel Brunet, B27-BP633, 86022 Poitiers, France

^b Laboratory of Electrochemistry, Corrosion and Energy Valorization, University of Béjaia, Rue de Targa Ouzemmour, 06000 Béjaia, Algeria

ARTICLE INFO

Article history:

Received 16 July 2013

Received in revised form 3 October 2013

Accepted 7 October 2013

Available online 14 October 2013

Keywords:

TiO_2

Sol-gel

Photoelectrochemistry

ORR

Substrate

ABSTRACT

In this study, mixed-oxides of $\text{Ti}_{1-x}\text{W}_x\text{O}_2$ ($0 \leq x \leq 0.3$) nanomaterials have been synthesized via a multistep sol-gel process. The effect of W doping on the anatase structure and on the electrical conductivity of the material was investigated. Photo-electrochemical action spectra and UV-vis spectroscopy were used to determine the band-gap energy of the mixed-oxides. The electrochemical stability of these materials was also investigated before they were tested as substrate for platinum nanocatalysts for oxygen reduction reaction. The metal was deposited onto the support either via the chemical route (carbonyl method) or via UV-irradiation.

© 2013 Elsevier B.V. All rights reserved.

1. Introduction

The widely used conventional support of Pt-based catalyst is carbon black (Vulcan XC-72). This latter, in low temperature fuel cells, is known to undergo electrochemical oxidation to surface oxides species and to CO_2 [1]. As carbon corrodes, noble metal nanoparticles on carbon black will detach from the electrode or aggregate to larger particles resulting in Pt surface area loss, which subsequently lowers the performance of PEMFCs [2]. Therefore, many efforts have been made to search for new catalyst supports [3]. Metal-metal oxide catalysts have been investigated as possible co-catalysts that are believed to operate via the bifunctional mechanism [4–6]. Tungsten oxide has been considered as a support material for fuel cell catalysts [7,8]. Titania, a widely used catalyst support [9], is known to enhance the activity in many cases due to the strong interaction between the active phase and the support [10]. In most of these oxides the metal is in its highest oxidation state and these materials are large-gap semiconductors. However, these oxides can be partially reduced [11] or doped with other metal cations [12], resulting in metal-like oxides. TiO_2 can be doped with other cations to prepare $\text{Ti}_{1-x}\text{M}_x\text{O}_2$, where M is a metal from group V or greater. Hence, doped TiO_2 has the possibility of being both electrically conducting and kinetically stable in aqueous acid or alkaline media

within a large electrode potential interval. The heteroatoms can be incorporated as a substituent of the titanium ion [13] or as an interstitial ion [14] of the titania lattice, or a surface-bound species, e.g., the surface wolframyl groups [15]. Depending on the nature and/or the history of sample preparation, the mode of incorporation of the heteroatom can change and, hence, the physical properties and the performances.

Various deposition techniques are available for the preparation of TiO_2 samples (powder or thin films), namely, magnetron sputtering [16], sol-gel [17], hydrothermal [18], chemical vapor deposition [19] or pulsed laser deposition [20]. Among them, sol-gel is of particular interest for its simplicity to obtain well-controlled stoichiometry doped TiO_2 oxides.

In the present work, tungsten was introduced to titania to obtain a mixed $\text{Ti}_{1-x}\text{W}_x\text{O}_2$ material, which was then characterized by various analytical and spectroscopic techniques. We are especially interested in the influence of W in the optoelectronic properties and in the interaction between platinum nanoparticles and the high-conducting mixed-oxide as support.

2. Experimental

2.1. Synthesis of materials by sol-gel synthesis

$\text{Ti}_{1-x}\text{W}_x\text{O}_2$ nanoparticles were synthesized via a sol-gel-based multistep synthesis involving firstly the dissolution of tungsten VI chlorides oxides WOCl_4 in isopropanol during 3 h under stirring at ambient temperature. Thereafter, the titanium isopropoxide (TIP) was added in this solution. Finally, after 16 h, a required quantity

* Corresponding author. Tel.: +33 54945 3625; fax: +33 54945 3580.

E-mail address: nicolas.alonso.vante@univ-poitiers.fr (N. Alonso-Vante).

¹ Present address: Institute of Technical Thermodynamics/Electrochemical Energy Technology, German Aerospace Center (DLR), Pfaffenwaldring 38-40, 70569 Stuttgart, Germany.

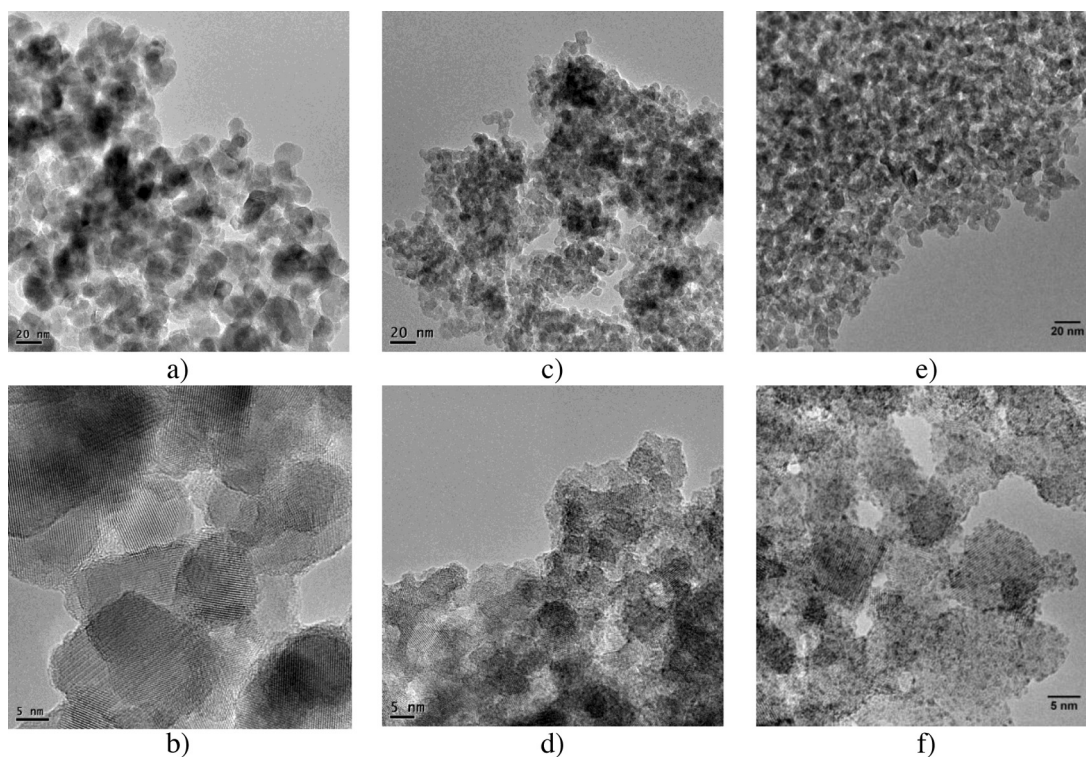


Fig. 1. TEM images of TiO_2 (a and b), $\text{Ti}_{0.95}\text{W}_{0.5}\text{O}_2$ (c and d) and $\text{Ti}_{0.7}\text{W}_{0.3}\text{O}_2$ (e and f) powders.

of water at 0°C was added to hydrolyze the TIP to $\text{Ti}_{1-x}\text{W}_x\text{O}_2$. The powder was obtained after evaporation of the solvent and dried under primary vacuum, and later heat-treated, under air or nitrogen, at 450°C , 1 h. The quantities of the chemical precursors vary according to the chosen molar ratio of Ti/W. For the sake of comparison, TiO_2 and WO_3 were independently synthesized using the sol–gel process.

2.2. Platinum nanoparticles supported onto oxides

For the synthesis of 8 wt.% Pt/oxide, platinum carbonyl $[\text{Pt}_3(\text{CO})_6]_5^{2-}$ was prepared by mixing 50.12 mg $\text{Na}_2\text{PtCl}_6 \cdot 6\text{H}_2\text{O}$ with 44.24 mg sodium acetate (mol ratio of $\text{NaAc}/\text{Pt}=6$) in methanol solution under CO atmosphere for 24 h. Subsequently, 200 mg of oxide $\text{Ti}_{0.8}\text{W}_{0.2}\text{O}_2$ was added to the above solution and stirred for another 12 h under nitrogen atmosphere. The final product ($\text{Pt}/\text{Ti}_{0.8}\text{W}_{0.2}\text{O}_2$) was collected on a Millipore filter membrane (dia. $0.22\ \mu\text{m}$ pore size), washed with water and dried in vacuum at room temperature [21,22].

2.3. Characterization of photocatalyst

The morphology and size of particles was examined with a TEM on a JEOL JEM-2001 equipped with a LaB_6 filament. The samples were characterized under an accelerating voltage of 200 kV and a resolution of ca. 0.19 nm.

The synthesized materials were characterized by powder X-ray diffraction using a diffractometer, Bruker “D8 Advance”, equipped with a linear detector fast VANTEC and a heating room Anton Paar (htk16) in the 2θ range of $15\text{--}70^\circ$. FullProf program suite was used for the Rietveld refinements.

Raman spectra were obtained with a spectrometer, Horiba Jobin Yvon “LabRam HR 800-UV”, using 0.05 mW green laser Ar^+ (Melles Griot), within the wave number range of $50\text{--}1200\ \text{cm}^{-1}$. The spectrometer is gauged with a sample of silicon with a resolution of

$0.5\ \text{cm}^{-1}$. The software LabSpec 5 allows for the acquisition and the treatment of the results.

The oxides were also analyzed by Diffuse Reflectance Spectroscopy with a spectrophotometer UV-Visible-PIR Varian “Cary 5000”, double UV-Visible-PIR beam (spectral range from 175 to 3300 nm) equipped with a Praying MantisTM. To determine the conductivity of oxide powders, the impedance spectroscopy measurements were recorded at room temperature. An Autolab potentiostat with a Frequency Response Analysis system software (FRA) was used to record the impedance in the frequency range of 50 kHz to 1 Hz, at a potential of 0 V. The cell used was provided with a two-gold disk electrodes compartment covered by a sheet of carbon, Toray. A torque of 25 in.-pounds assured the electrical contact and reproducibility of the measurements of the various oxides powders. All generated data showed a non-frequency dependence.

2.4. Photoelectrochemical and electrochemical measurements

Photocurrent measurements were performed at room temperature in a photoelectrochemical cell (PEC) provided with three electrodes. A plate of glassy carbon served as counter electrode, and a reversible hydrogen electrode (RHE), connected to the cell compartment through a Luggin capillary, as a reference electrode. A solution 0.5 M H_2SO_4 was used as electrolyte. The working (photo)electrodes were prepared by spin coating (at 3500 rpm) using a suspension of the oxides in ethanol (5 mg/mL) and deposited on $\text{SnO}_2\text{:F}$ (Solems) substrates of $0.5\ \text{cm}^2$. After ejection and evaporation of the solvent, a porous $\text{Ti}_{1-x}\text{W}_x\text{O}_2$ adherent thin film was formed. The samples were calcined afterwards, in air at 450°C . The PEC was provided with a quartz window and was placed on an optical table on a support that allowed the displacement of all the system in X, Y and Z directions. The measurements were carried under UV–vis illumination and in darkness. The UV–vis source of light was from a Xenon lamp, Spectral products ASB-XE-175. Current–potential curves were performed in Ar-saturated electrolyte, from 0.1 to 2 V/RHE at $50\ \text{mV s}^{-1}$.

For the oxygen reduction reaction (ORR) measurements, the working electrode was a glassy carbon disk with a 3 mm diameter (geometric surface area, 0.071 cm^2) and polished with Al_2O_3 (5A) powder prior to catalyst deposition. The catalyst ink was prepared by dispersing 10 mg of catalysts, e.g., $\text{Ti}_{0.8}\text{W}_{0.2}\text{O}_2$, 8 wt.% Pt/ $\text{Ti}_{0.8}\text{W}_{0.2}\text{O}_2$ (by carbonyl way) and 8 wt.% Pt/ $\text{Ti}_{0.8}\text{W}_{0.2}\text{O}_2$ (by photodeposition), in $250 \mu\text{L}$ Nafion® (5 wt.% in water/aliphatic alcohol solution, Aldrich) and $1250 \mu\text{L}$ ultra pure water ($18 \text{ M}\Omega\text{-cm}$) in an ultrasound bath for 1 h. A drop of $3.0 \mu\text{L}$ of catalyst ink was deposited onto the working electrode surface and dried under nitrogen. Before the ORR measurements, cyclic voltammetry, in nitrogen-saturated electrolyte, was performed to clean and activate the electrode surface from 0.05 to 1.2 V/RHE at 50 mV s^{-1} . 20 cycles were necessary to stabilize the current–potential signal. Linear current–potential curves were recorded from 1.0 to 0.2 V/RHE in oxygen-saturated electrolyte at a 1600 rpm rotating speed. All electrochemical measurements were recorded with a Potentiostat, Autolab PGSTAT30.

3. Results and discussion

3.1. TEM characterization of the $\text{Ti}_{1-x}\text{W}_x\text{O}_2$ powders

Fig. 1 shows low and high magnification TEM images of some $\text{Ti}_{1-x}\text{W}_x\text{O}_2$ powders. For each sample the size of particles is clearly in the order of ca. 10 nm. Whatever the considered sample, TEM observations did not show the presence of larger particles. The particles seem to be regular in shape regardless of the W-content. From Fig. 1a, c and e, it seems that the addition of W is responsible for a slight decrease in the mean particle size. Furthermore, for high W-content (i.e. for $\text{Ti}_{0.7}\text{W}_{0.3}\text{O}_2$ sample), small particles are apparent (Fig. 1e). The presence of these particles could be attributed to the growth of small clusters at the surface of larger ones.

3.2. Phase identification in the prepared $\text{Ti}_{1-x}\text{W}_x\text{O}_2$ materials

The Fig. 2 summarizes the XRD patterns of the whole set of synthesized oxides, namely, $\text{Ti}_{0.7}\text{W}_{0.3}\text{O}_2$, $\text{Ti}_{0.8}\text{W}_{0.2}\text{O}_2$, $\text{Ti}_{0.9}\text{W}_{0.1}\text{O}_2$, $\text{Ti}_{0.95}\text{W}_{0.05}\text{O}_2$, $\text{Ti}_{0.99}\text{W}_{0.01}\text{O}_2$, and TiO_2 . The vertical bars at the bottom show the diffraction peaks corresponding to the anatase and brookite phase of TiO_2 . The anatase phase is the predominant phase on all synthesized samples. The visible peak at $2\theta = 31^\circ$ corresponding to brookite phase disappears with the tungsten concentration ($>1\%$). This result supports the fact that tungsten inhibits any phase change of anatase [23]. Moreover, up to a W content of 30 at.%, there is no formation of crystalline WO_3 phase, which can suggest that W could be built-in in the matrix of TiO_2 . Structural analysis of the $\text{Ti}_{1-x}\text{W}_x\text{O}_2$ material with different W contents calcined at 450°C suggests that the anatase phase of titanium dioxide does not change when reacting with a tungstate chemical precursor for W content lower than 30 at.%.

3.3. Structural characterization of $\text{Ti}_{1-x}\text{W}_x\text{O}_2$ materials and effect of the heat-treatment

In addition, tungsten is responsible for shifting diffraction peaks of anatase toward lower angles. Diffractograms shown in Fig. 2 were fitted by the Fullprof free software and Rietveld structure refinement. The average crystallite size as well as lattice parameters of $\text{Ti}_{1-x}\text{W}_x\text{O}_2$ with ($0 \text{ at.\%} < \text{W} < 30 \text{ at.\%}$) obtained from these simulations are summarized in Table 1. The lattice parameters ($a=b$, and c) show variations with the W-content. While the a -parameter monotonously increases with the W-content, the c -parameter decreases. As a result, the volume unit cell increases until 10 at.% W, and then remains nearly constant. Furthermore, it can be pointed out that the addition of a small amount of W (1 at.%) produces a

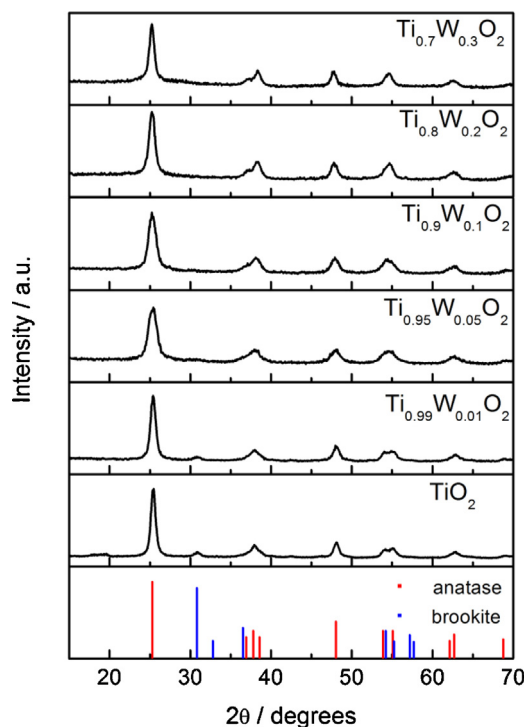


Fig. 2. XRD patterns of $\text{Ti}_{0.7}\text{W}_{0.3}\text{O}_2$, $\text{Ti}_{0.8}\text{W}_{0.2}\text{O}_2$, $\text{Ti}_{0.9}\text{W}_{0.1}\text{O}_2$, $\text{Ti}_{0.95}\text{W}_{0.05}\text{O}_2$, $\text{Ti}_{0.99}\text{W}_{0.01}\text{O}_2$ and TiO_2 . Vertical bars at the bottom represent the diffraction peaks positions of anatase and brookite phases.

slight shrinkage of both a , and c parameters (in comparison with TiO_2 sample) which could be associated with the substitution of Ti^{4+} by W^{6+} . As a result of this substitution, a defect formation occurs at the metal sites [24].

The effect of the calcination temperature was also in situ XRD examined on $\text{Ti}_{0.8}\text{W}_{0.2}\text{O}_2$ and the $\text{Ti}_{0.2}\text{W}_{0.8}\text{O}_2$ samples see Fig. 3. The as-prepared sample: $\text{Ti}_{0.8}\text{W}_{0.2}\text{O}_2$ shows broad diffraction patterns characteristic of the anatase crystal phase with a low crystallinity at ambient temperature as shown in Fig. 3 (lower panel). With the increase of the calcination temperature (i.e. 650°C), the narrowing of the diffraction peaks was observed, thus crystallite growth of the titanium dioxide takes place. However, the appearance of a shoulder at 24° testifies of a phase change, which is clearly put in evidence when measuring the heat-treated sample at 30.3°C , see upper panel of Fig. 3.

3.4. Strains analyses of $\text{Ti}_{1-x}\text{W}_x\text{O}_2$ materials

To complete the structural study of the $\text{Ti}_{1-x}\text{W}_x\text{O}_2$ materials ($x < 0.3$), Raman spectra were generated on those samples and contrasted in Fig. 4A. These results are consistent with the phase analysis realized from data obtained by XRD. All $\text{Ti}_{1-x}\text{W}_x\text{O}_2$ samples showed the characteristic peaks for the E_g , B_{1g} , A_{1g} and E_g modes of anatase, but their positions slightly deviate from those of bulk anatase at 145, 398, 519 and 639 cm^{-1} [25]. The samples with W content below 5 at.% show peaks at 247, 323 and 366 cm^{-1} that can be assigned to the A_{1g} , B_{1g} , and B_{2g} modes of brookite [26] (Fig. 4B). Other details observed in the Raman spectra is the broad emission peak centered at ca. 972 cm^{-1} for W-content higher than 1 at.% (Fig. 4C). The magnitude of this peak increases as the W content increases. There is no indication of other tungsten species, including crystalline WO_3 . This is fairly in agreement with conclusions drawn from XRD experiments. Consequently, this peak is attributed to the $\text{W}=\text{O}$ stretching mode of surface wolframyl entities [27]. In order to determine the effects of tungsten on the

Table 1
Characterization data of the different tungsten doped titanium oxide samples.

Sample	Crystallite size (XRD)/nm	a (= b)/Å	c /Å	Cell volume/Å ³	Crystallite size (Raman)/nm	Tensile stress/MPa	Compressive stress/MPa	E_{gap} (eV) Kubelka–Munk	E_{gap} (eV) action spectrum	Conductivity (mS/cm)
TiO ₂	9.8	3.785	9.483	135.856	10.1	857	–	3.44	3.42	1.77×10^{-3}
Ti _{0.99} W _{0.01} O ₂	10.5	3.784	9.478	135.712	9.4	791	–	3.31	–	45.4×10^{-3}
Ti _{0.95} W _{0.05} O ₂	6.4	3.789	9.482	136.130	6.4	–	332	–	3.38	2.62
Ti _{0.9} W _{0.1} O ₂	7.2	3.796	9.473	136.502	6.1	–	674	–	–	88.5
Ti _{0.8} W _{0.2} O ₂	9.1	3.801	9.431	136.255	5.4	–	63	3.37	–	147.06
Ti _{0.7} W _{0.3} O ₂	10.8	3.807	9.422	136.555	5.3	–	579	–	–	–
WO ₃	–	–	–	430.059	–	–	–	2.91	3.05	–

microstructure of TiO₂, the frequency shift and full width at half maximum (FWHM) of the E_g mode at ca. 144 cm^{-1} are plotted in Fig. 5A. Within the W-content range from 0 to 30 at.%, the full-width at half-maximum of the peak increases from 12.6 to 29.9 cm^{-1} . At the same time, the E_g band is blue-shifted from 144.6 to 155.3 cm^{-1} . These data are consistent with a monotonous decrease of the mean crystallite size as the W content increases. There are apparently some discrepancies between XRD calculations and the Raman data since the crystallite size of anatase phase calculated from diffractograms continuously decreases up to a W content of 10 at.% and then increases. Such difference is due to the fact that XRD data reflect the overall size of crystallites including heavily tungsten-doped surfaces of TiO₂ nanocrystals observed for high W-content samples and that Raman data reflect the properties of the TiO₂ core for samples exhibiting wolframyl groups on their surface [24]. Our observed E_g mode blue-shift could be attributed to the effect of tungsten into the matrix of anatase and consequently associated with the metal-ions insertion [28]. Yang et al. [29] believe that the blue-shift of the peak could be caused by the residual compressive strain, while the broadening of the peak may be associated with defects such as dislocation and oxygen vacancies leading to a deteriorated crystal quality. The magnitude of the stress affecting TiO₂ grains has been estimated from Raman spectra using the procedure

reported by Kim et al. [24]. For each sample, the crystallite size was first obtained from the E_g mode bandwidth by using the phonon confinement model [30]. The expected position of the E_g mode was then deduced from the calculated TiO₂ crystallite size. Finally, the difference between the expected and the observed E_g mode peak position was then used to estimate the nature (tensile or compressive) and the magnitude of the stress affecting the material by using the slope of $3.16 \text{ cm}^{-1}/\text{GPa}$ [24,31]. Results obtained are summarized in Table 1. From Table 1 one observes that the stress affecting the sample can be either a tensile or a compressive one as a function of its composition. For low W content samples (i.e. $W < 1 \text{ at.}\%$), the stress affecting the anatase phase is a tensile one. This stress can be associated with the presence of the brookite phase suggesting the larger strain between TiO₂ grains [32]. The samples with $W > 5 \text{ at.}\%$ are subjected to a compressive stress. This is due to the surface segregation of parasitic phases imposing large compressive strain to the TiO₂ layer, and to the lattice of TiO₂ that simultaneously experiences excessive defects. This latter effect is however balanced by the expansion of the anatase lattice.

From the Rietveld refinement results, we obtained the variations of the Ti–O bond distances with the W-content. The anatase structure can be described as edge-sharing of identical TiO₆ octahedral. The octahedral is elongated along the c -axis to result in four short equatorial Ti–O bonds and two long axial Ti–O bonds. Fig. 5B shows the variations of the Ti–O bond distances of anatase with the tungsten content. The axial bond remains more or less constant and decreases significantly for 30 at.% W, while the equatorial bond shows a monotonous increase with the increase of the W-content.

Based on the above discussion, it is very likely that two tungsten species are the lattice doping tungsten and the surface wolframyl group. When the W-content is low (i.e. lower than 5 at.%), most of the tungsten species are majorly inside the anatase lattice and substitute the titanium ions. From Raman experiments, the saturation point can be estimated to be between 1 and 5 at.% since the presence of wolframyl species is visible at W content higher than 5 at.%. This saturation range is slightly lower than other already published data [24,33,34]. In fact, at higher tungsten content (i.e. higher than 5 at.%), the additional tungsten atoms are responsible for the formation of surface bonded wolframyl groups, as evidenced by the growth of the 972 cm^{-1} peak in the Raman spectra. It can be seen in Table 1 that both a , and c parameters are slightly decreased by simply adding 1 at.% of W. Similar observations were done by Kim et al. [24]. The addition of 5 at.% of W, both a -, and c -parameters expand. This can be explained by the substitution of Ti^{4+} by W^{6+} in agreement with the explanation given by Kim et al. [24]. As the surface bound wolframyl groups become visible (i.e. for W content higher than 5 at.%), the lattice is expanded in the direction of a -parameter, whereas there is a shrinkage along the c -axis. As conclusion, it seems that surface groups are responsible for expanding the lattice along the a -axis, and the c -parameter decreases in order to keep the cell volume at a nearly constant value as shown in Table 1. Other causes such as surface hydration effect or repulsive interactions of the parallel surface defect dipoles can also be responsible for lattice volume changes [35,36]. However, the first

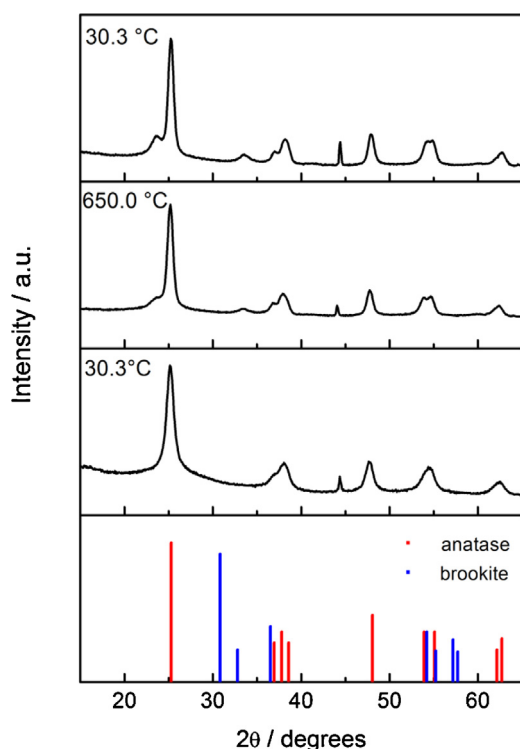


Fig. 3. XRD pattern evolution of Ti_{0.8}W_{0.2}O₂, during the in situ heat-treatment in air (30.3–650 °C), from bottom to upper panel.

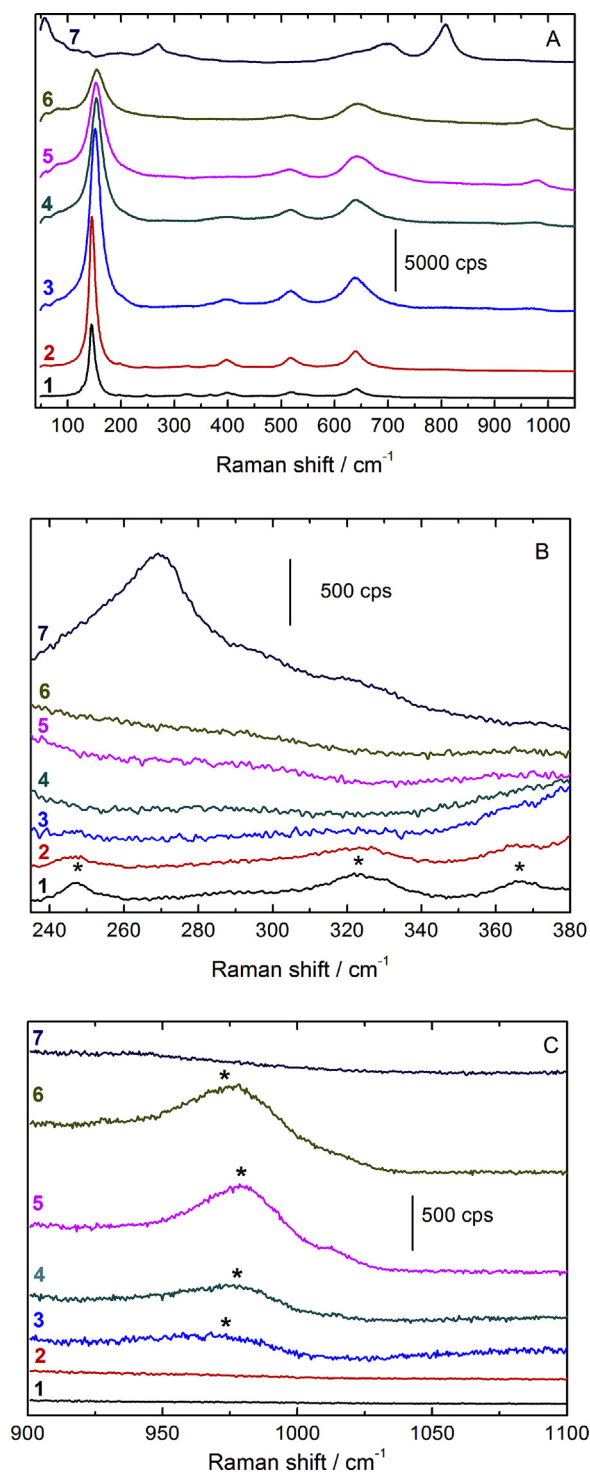


Fig. 4. (A) Raman spectra of oxides, and tungsten mixed-oxide in the spectral range of 40–1050 cm^{-1} . (B) Raman spectra in the energy interval of 240–380 cm^{-1} showing the evolution of the brookite phase. Bands associated to the A_{1g} , B_{1g} , and B_{2g} modes of brookite are marked with stars. (C) Raman spectra in the energy interval of 900–1100 cm^{-1} showing the evolution of wolframyl groups. The band attributed to the W=O stretching mode of surface wolframyl entities is marked with a star. 1: TiO_2 ; 2: $\text{Ti}_{0.99}\text{W}_{0.01}\text{O}_2$; 3: $\text{Ti}_{0.95}\text{W}_{0.05}\text{O}_2$; 4: $\text{Ti}_{0.9}\text{W}_{0.1}\text{O}_2$; 5: $\text{Ti}_{0.8}\text{W}_{0.2}\text{O}_2$; 6: $\text{Ti}_{0.7}\text{W}_{0.3}\text{O}_2$; 7: WO_3 .

phenomenon would be responsible for a lattice contraction as the particle size decreases. Furthermore a lattice expansion would be observed as a result of the repulsive interaction between surface defect dipoles. Additionally, since the polarizability of the anatase lattice is low it is possible to conclude that repulsive interactions

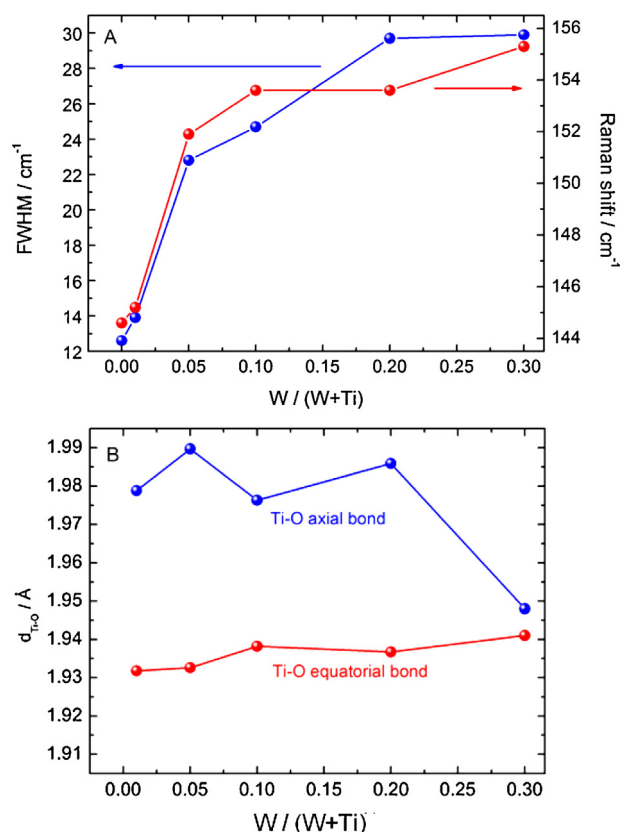


Fig. 5. (A) Variation of the peak position (red line) and the peak width (blue line) of the E_g band of titanium dioxide with the tungsten at.% content. (B) Variations of the Ti–O (axial–equatorial) bond distances of titanium dioxide with the tungsten at.% content. (For interpretation of the references to color in this figure legend, the reader is referred to the web version of the article.)

able of exerting a negative pressure on the crystal lattice are weak [35].

3.5. Light absorption properties

The samples of $\text{Ti}_{1-x}\text{W}_x\text{O}_2$ were measured by reflectance technique and then adjusted using a Kubelka–Munk transformation. Determination of the band-gap energy was essential to identify changes in the electronic structure of the oxides, which depends on the structural properties. Fig. 6A shows the reflectance spectra of TiO_2 , $\text{Ti}_{0.99}\text{W}_{0.01}\text{O}_2$, $\text{Ti}_{0.8}\text{W}_{0.2}\text{O}_2$ and WO_3 . One can see that all titanium-based oxides are transparent in the visible light region. Due to the fundamental absorption in the vicinity of band-gap, the reflectance increases abruptly as the wavelength reaches the visible range. The reflectance maximum decreases with the W-content, suggesting changes in the opto-electronic properties. Fig. 6B shows the direct transition Kubelka–Munk plot as a function of the photon energy allowing the estimation at the intercept of the threshold energies, namely, 3.31; 3.37; 3.44; and 2.91 eV for $\text{Ti}_{0.99}\text{W}_{0.01}\text{O}_2$, $\text{Ti}_{0.8}\text{W}_{0.2}\text{O}_2$, TiO_2 , and WO_3 , respectively. The apparent decrease in the overall band gap energy with the amount of tungsten doping testifies a shift to the visible region. Moreover, as discussed below, the increase of the conductivity (Table 1) with the tungsten content confers to such mixed-oxides a metal-like behavior. In other words, the increase in the conductivity is the result of the effect of the electronic state of W in the band structure of TiO_2 and can also be related to the constancy of the long Ti–O bond length in the crystal structure.

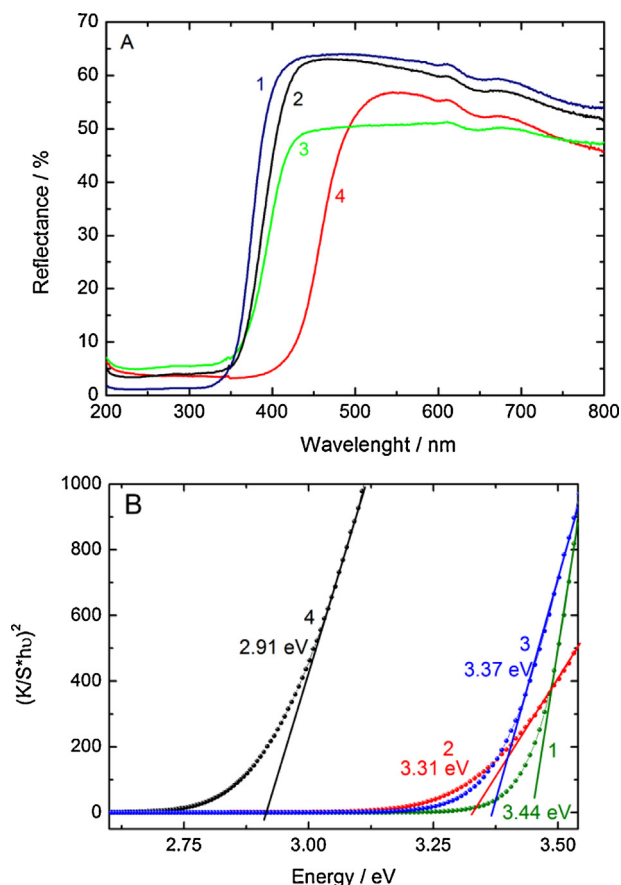
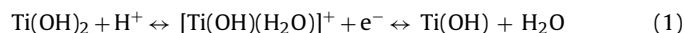


Fig. 6. (A) UV-visible diffuse reflectance spectra of selected samples **1**: TiO_2 , **2**: $\text{Ti}_{0.99}\text{W}_{0.01}\text{O}_2$, **3**: $\text{Ti}_{0.8}\text{W}_{0.2}\text{O}_2$ and **4**: WO_3 . (B) The corresponding Kubelka-Munk-transformed diffuse reflectance as a function of $h\nu$ for a direct allowed transition.

3.6. Photoelectrochemistry

The current–potential curves of $\text{Ti}_{0.95}\text{W}_{0.05}\text{O}_2$, $\text{Ti}_{0.9}\text{W}_{0.1}\text{O}_2$ and $\text{Ti}_{0.8}\text{W}_{0.2}\text{O}_2$ porous oxide films, measured in darkness and under UV–vis illumination are shown in Fig. 7A. The current responses are mainly dominated by the characteristic redox peaks of Ti^{4+} and Ti^{3+} (hydr)oxide species of TiO_2 occurring in the potential window from 0.05 and 0.6 V vs. RHE [37]:



However, the electron–hole recombination increases with at.% of W-content and thus the photocurrent (i_{ph}) is greatly reduced. This fact allows ruling out the presence of amorphous WO_3 phase which would be responsible for increasing the magnitude of the photocurrent response [38]. This doping effect of 3d metals has been studied by DFT (density functional theory) calculations on TiO_2 (rutile) doped with W [39], Mo [40], Fe, Co, Ni, Mn [41]. According to such calculations a strong hybridization with the doping elements appears in the band gap of TiO_2 leading to the formation of intermediate energy states. As demonstrated in the present work, the consequence of such phenomenon is not the decrease of the fundamental energy gap of the mixed-oxide, cf. Fig. 6, but the increase of the electrical conductivity, cf. Table 1. The photogenerated electron–hole (e–h) pairs on $\text{Ti}_{0.8}\text{W}_{0.2}\text{O}_2$ only take place under UV irradiation, Fig. 7B. At a relatively high applied electrode potential (1 V vs. RHE) the recombination of e^- – h^+ pairs is evident under chopped illumination at intervals of 5 s. Nonetheless, as depicted in the insert of Fig. 7A, it is clear that the photo-response decreases with the increase of the W content. This is concomitant with the increase of the electronic conductivity, cf. Table 1, and further in

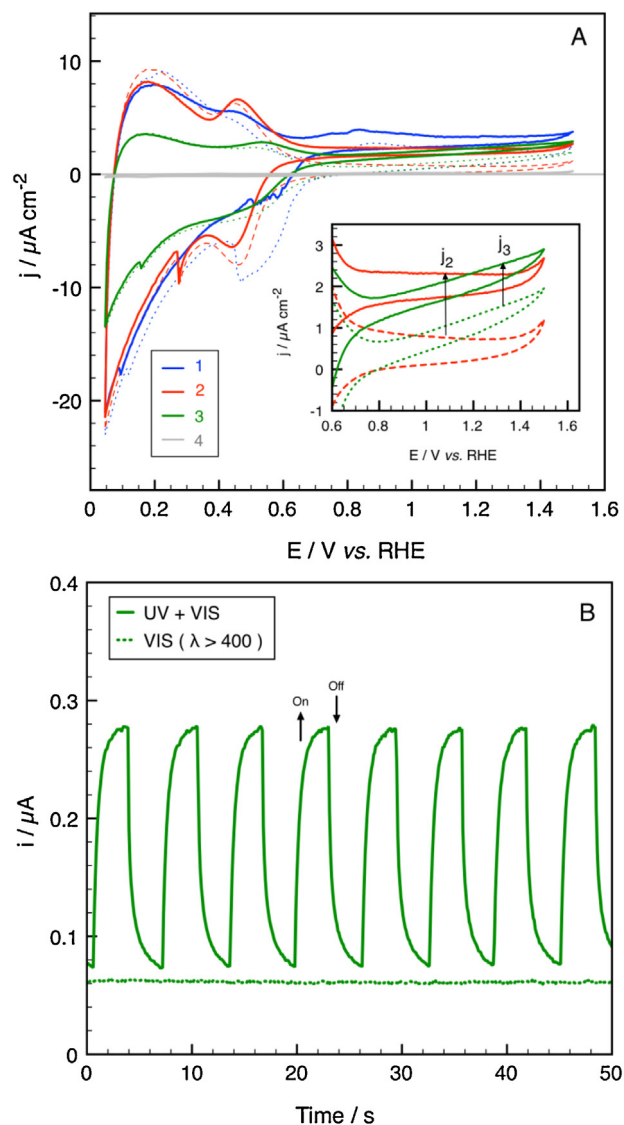


Fig. 7. (A) Current–potential characteristics of selected samples: **1**: $\text{Ti}_{0.95}\text{W}_{0.05}\text{O}_2$, **(2)** $\text{Ti}_{0.9}\text{W}_{0.1}\text{O}_2$, **3**: $\text{Ti}_{0.8}\text{W}_{0.2}\text{O}_2$ and **4**: SnO_2 :F substrate in darkness (dashed lines) and under UV (full lines). The insert zooms the photo-response of j_3 : $\text{Ti}_{0.8}\text{W}_{0.2}\text{O}_2$ and j_4 : $\text{Ti}_{0.9}\text{W}_{0.1}\text{O}_2$. The periodic on-off photocurrent response of $\text{Ti}_{0.8}\text{W}_{0.2}\text{O}_2$ at $E = 1$ V vs. RHE, under UV and visible ($\lambda > 400$ nm) irradiation is shown in (B). Measurements were carried out in Ar-saturated 0.5 M H_2SO_4 electrolyte with a scan rate of 50 mV s^{-1} .

good agreement with a similar trend observed in TiO_2 thin films doped with W, deposited by magnetron sputtering technique [16].

The modification of the band structure of TiO_2 by the insertion of W in the crystal structure was further studied by measuring i_{ph} with respect to wavelength of the incident photons, Fig. 8A. The direct band gap (E_g) of the oxides was estimated through $(i_{\text{ph}} h\nu)^2$ vs. $h\nu$ according the equation:

$$i_{\text{ph}} = A \frac{(h\nu - E_g)^n}{h\nu} \quad (2)$$

where h is the Planck constant ($6.63 \times 10^{-34} \text{ Js}$), ν the photon frequency (Hz), n the order of optical transition and A is a constant that depends on the optical transition. For $n = 1/2$, see, Fig. 8B. For the reference materials WO_3 and thermal treated TiO_2 (anatase), a band gap of 3.05 eV and 3.32 eV was obtained, respectively. The intersection of the fitting line of $\text{Ti}_{0.8}\text{W}_{0.2}\text{O}_2$ was not straight forward (inset Fig. 8B), indicating again the introduction of intermediate states into the forbidden gap. Data are summarized in Table 1.

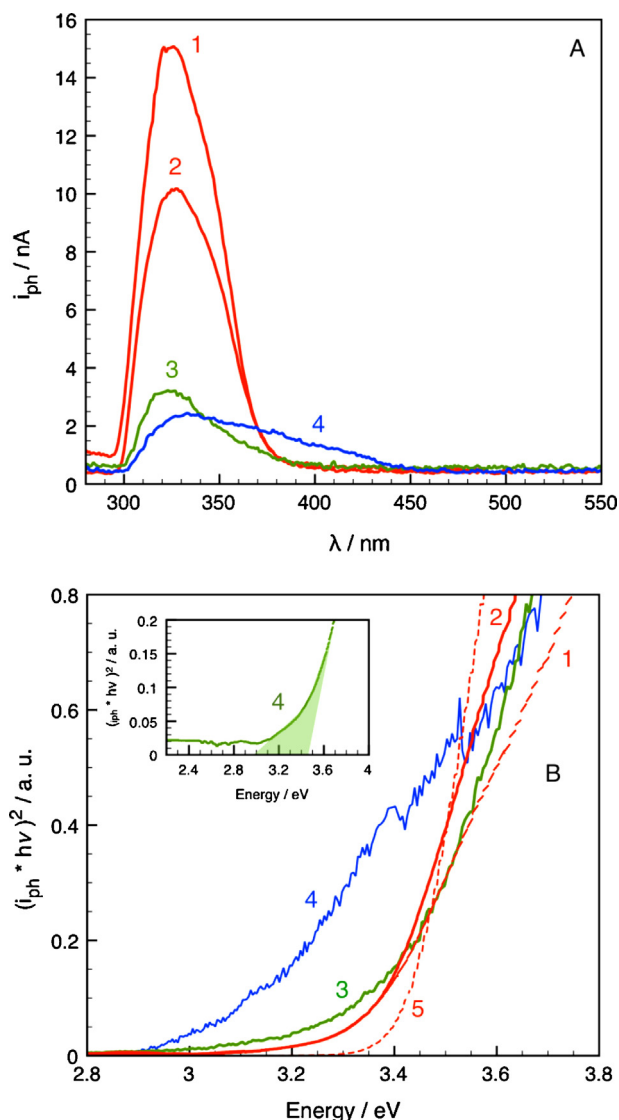


Fig. 8. (A) Photo-current action spectra of the selected samples: **1:** TiO_2 (thermal treated) **2:** TiO_2 (as prepared), **3:** $\text{Ti}_{0.8}\text{W}_{0.2}\text{O}_2$ and **4:** WO_3 porous film electrodes deposited on $\text{SnO}_2:\text{F}$ substrate, measured at 1 V vs. RHE in Ar-saturated 0.5 M H_2SO_4 solution under UV–vis illumination. (B) Plots of $(i_{\text{ph}} \cdot hv)^2$ vs. hv to determine the band gap (E_g). **5:** Commercial TiO_2 Degussa P25 with a ratio of anatase to rutile phases of 3:1 is plot for comparison. The inset shows the wide energy range of intersection for another electrode of **4:** $\text{Ti}_{0.8}\text{W}_{0.2}\text{O}_2$.

As a final point the current potential curves of porous $\text{Ti}_{0.8}\text{W}_{0.2}\text{O}_2$ electrode, measured up to 2 V vs. RHE at 20 mV s^{-1} , are shown in Fig. 9. Transpassive corrosion of the electrode during O_2 -evolution was observed beyond 1.5 V vs. RHE in either darkness or under UV–vis illumination. In this sense the material exhibits similar stability than TiO_2 in acid medium, but with an enhanced metallic character. Consequently, the nanostructured powder of $\text{Ti}_{0.8}\text{W}_{0.2}\text{O}_2$ can be a promising ceramic substrate for electrocatalytic nanoparticles of Pt [42] or Ir-based [43] used as oxygen electrodes of PEM fuel cells and electrolyzers, respectively.

3.7. Oxygen reduction reaction (ORR)

Tafel plots extracted from ORR curves registered in an oxygen saturated acid electrolyte solution are summarized in Fig. 10. This figure contrasts the activity of two substrates: glassy carbon, and $\text{Ti}_{0.8}\text{W}_{0.2}\text{O}_2$ where it is clearly put in evidence the low catalytic activity of these substrate materials toward the ORR in 0.5 M H_2SO_4 .

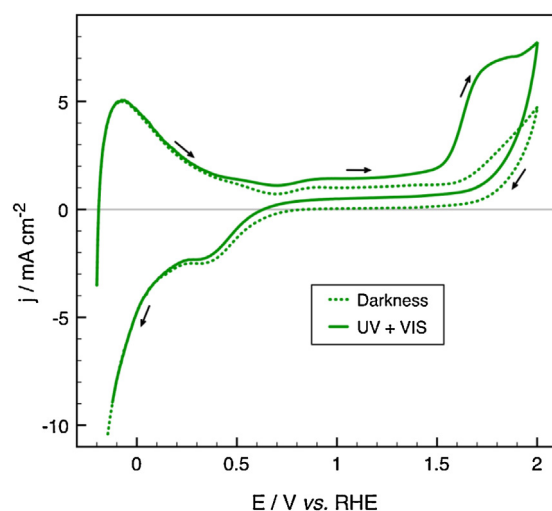


Fig. 9. Current–potential curves of $\text{Ti}_{0.8}\text{W}_{0.2}\text{O}_2$ electrode up to 2 V vs. RHE, in Ar-saturated 0.5 M H_2SO_4 solution in darkness (full line) and under UV–vis radiation (dashed line). The arrows indicate the sense of the potential sweep, which was performed at 20 mV s^{-1} .

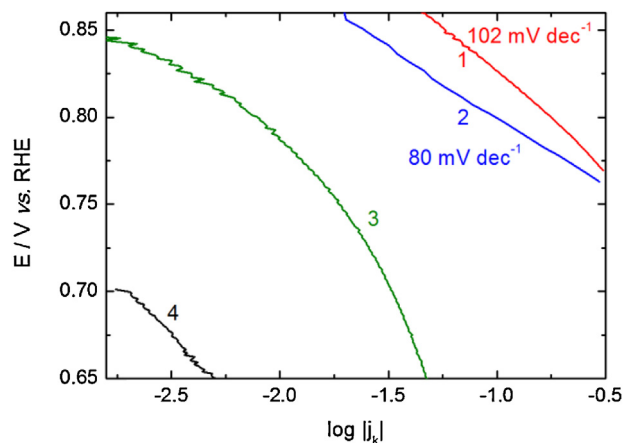


Fig. 10. Tafel plots obtained from ORR curves registered in an oxygen saturated electrolyte (H_2SO_4 0.5 M) at a scan rate of 5 mV s^{-1} with **1:** $\text{Pt}/\text{Ti}_{0.8}\text{W}_{0.2}\text{O}_2$, **2:** Pt/C , **3:** $\text{Ti}_{0.8}\text{W}_{0.2}\text{O}_2$, **4:** glassy carbon.

The chemical route (carbonyl way) was used to deposit platinum nanoparticles both on Vulcan and on $\text{Ti}_{0.8}\text{W}_{0.2}\text{O}_2$ substrates. One can clearly see the enhancement of the reaction kinetics when platinum is deposited onto the oxide substrate. Furthermore, Tafel slopes determined for both samples show a slight deviation from the theoretical value of 120 mV dec^{-1} [44,45]. This result reflects different adsorption isotherms and could be related to different adsorption rates of oxygen on the catalyst surface [46]. Additionally, this fact is fairly in agreement with kinetic currents values calculated at 0.85 V vs. RHE for Pt/C and $\text{Pt}/\text{Ti}_{0.8}\text{W}_{0.2}\text{O}_2$ catalysts. They are respectively of $15 \mu\text{A cm}^{-2}_{\text{Pt}}$ and $29 \mu\text{A cm}^{-2}_{\text{Pt}}$ which means that a two-fold enhancement factor in the ORR kinetics can be obtained by depositing platinum onto tungsten doped titania substrate.

4. Conclusion

In this study TiO_2 nanomaterials containing different amount of tungsten have been synthesized via a multistep sol–gel process. These samples exhibit a composition dependent structure. Depending on the tungsten amount, lattice and surface doping species

can be deduced. At low tungsten content W is mainly incorporated into the anatase lattice which results in the expansion of the TiO₂ lattice. At a high tungsten-content (i.e. W > 5 at.%), the formation of surface-bonded wolframyl groups takes place. These surface wolframyl groups are responsible for compressing the TiO₂ core thus a compressive strain. Furthermore, the magnitude of the photocurrent response under UV illumination decreases as the amount of tungsten doping species increases. This phenomenon can be explained by the reduction of the overall energy band gap and the introduction of intermediate states into the forbidden gap near the conduction band of TiO₂ as well as by the distortion of the anatase crystal caused by surface wolframyl groups leading to changes in the electronic structure of anatase. This is also responsible for increasing the electronic conductivity of the oxides up to 147 mS·cm⁻¹ for a tungsten content of 20 at.%. The latter property is of great interest for electrocatalytic applications since these materials can act as a substrate to deposit electrocatalytic nanomaterials such as platinum nanoparticles. Moreover the electrochemical stability of these W-TiO₂ nanomaterials up to potentials such as 1.5 V vs. RHE allows envisioning their application in a wide range of electrochemical energy conversion devices.

Acknowledgments

This work was partially supported by the European Union's Seventh Framework Programme (FP7/2007–2013) for the Fuel Cell and Hydrogen Joint Technology Initiative under grant agreement n° 303492 CathCat. Aldo Gago thanks CONACYT for financial support (Scholarship 305477).

References

- [1] K.H. Kangasniemi, D.A. Condit, T.D. Jarvi, *Journal of the Electrochemical Society* 151 (2004) E125–E132.
- [2] J. Liu, Z. Zhou, X. Zhao, Q. Xin, G. Sun, B. Yi, *Physical Chemistry Chemical Physics* 6 (2004) 134–137.
- [3] R. Borup, J. Meyers, B. Pivovar, Y.S. Kim, R. Mukundan, N. Garland, D. Myers, M. Wilson, F. Garzon, D. Wood, P. Zelenay, K. More, K. Stroh, T. Zawodzinski, J. Boncella, J.E. McGrath, M. Inaba, K. Miyatake, M. Hori, K. Ota, Z. Ogumi, S. Miyata, A. Nishikata, Z. Siroma, Y. Uchimoto, K. Yasuda, K.-I. Kimijima, N. Iwashita, *Chemical Reviews* 107 (2007) 3904–3951.
- [4] K. Lasch, L. Jörissen, J. Garche, *Journal of Power Sources* 84 (1999) 225–230.
- [5] E.J. McLeod, V.I. Birss, *Electrochimica Acta* 51 (2005) 684–693.
- [6] J.W. Long, R.M. Stroud, K.E. Swider-Lyons, D.R. Rolison, *Journal of Physical Chemistry B* 104 (2000) 9772–9776.
- [7] P.K. Shen, A.C.C. Tseung, *Journal of the Electrochemical Society* 141 (1994) 3082–3090.
- [8] M. Götz, H. Wendt, *Electrochimica Acta* 43 (1998) 3637–3644.
- [9] L. Timperman, A. Lewera, W. Vogel, N. Alonso-Vante, *Electrochemistry Communications* 12 (2010) 1772–1775.
- [10] M. Gopal, W.J. Moberly Chan, L.C. De Jonghe, *Journal of Materials Science* 32 (1997) 6001–6008.
- [11] T. Ioroi, H. Senoh, S.-I. Yamazaki, Z. Siroma, N. Fujiwara, K. Yasuda, *Journal of the Electrochemical Society* 155 (2008) B321–B326.
- [12] C.V. Subban, Q. Zhou, A. Hu, T.E. Moylan, F.T. Wagner, F.J. DiSalvo, *Journal of the American Chemical Society* 132 (2010) 17531–17536.
- [13] L.G. Devi, B. Nagaraj, K.E. Rajashekhar, *Chemical Engineering Journal* 181–182 (2012) 259–266.
- [14] M. Acikgoz, P. Gnutek, C. Rudowicz, *Chemical Physics* 402 (2012) 83–90.
- [15] C.W. Lai, S. Sreekantan, *International Journal of Hydrogen Energy* 38 (2013) 2156–2166.
- [16] G. Abadias, A.S. Gago, N. Alonso-Vante, *Surface and Coatings Technology* 205 (2011) S265–S270.
- [17] Q. Li, D.J.G. Satur, H. Kim, H.G. Kim, *Materials Letters* 76 (2012) 169–172.
- [18] D. Ke, H. Liu, T. Peng, X. Liu, K. Dai, *Materials Letters* 62 (2008) 447–450.
- [19] A. Sobczyk-Guzenda, M. Gazicki-Lipman, H. Szymanowski, J. Kowalski, P. Wojciechowski, T. Halamus, A. Tracz, *Thin Solid Films* 517 (2009) 5409–5414.
- [20] Y. Suda, H. Kawasaki, T. Ueda, T. Ohshima, *Thin Solid Films* 475 (2005) 337–341.
- [21] S. Mokrane, L. Makhlofi, N. Alonso-Vante, *Journal of Solid State Electrochemistry* 12 (2008) 569–574.
- [22] L. Timperman, Y.J. Feng, W. Vogel, N. Alonso-Vante, *Electrochimica Acta* 55 (2010) 7558–7563.
- [23] S. Komornicki, M. Radecka, P. Sobaś, *Journal of Materials Science: Materials in Electronics* 15 (2004) 527–531.
- [24] D.-S. Kim, J.-H. Yang, S. Balaji, H.-J. Cho, M.-K. Kim, D.-U. Kang, Y. Djaoued, Y.-U. Kwon, *CrystEngComm* 11 (2009) 1621–1629.
- [25] T. Ohsaka, F. Izumi, Y. Fujiki, *Journal of Raman Spectroscopy* 7 (1978) 321–324.
- [26] G.A. Tompsett, G.A. Bowmaker, R.P. Cooney, J.B. Metson, K.A. Rodgers, J.M. Seakins, *Journal of Raman Spectroscopy* 26 (1995) 57–62.
- [27] F.D. Hardcastle, I.E. Wachs, *Journal of Raman Spectroscopy* 26 (1995) 397–405.
- [28] Z.-M. Wang, G. Yang, P. Biswas, W. Bresser, P. Boolchand, *Powder Technology* 114 (2001) 197–204.
- [29] Y. Yang, Q. Zhang, B. Zhang, W.B. Mi, L. Chen, L. Li, C. Zhao, E.M. Djalio, X.X. Zhang, *Applied Surface Science* 258 (2012) 4532–4537.
- [30] S. Kelly, F.H. Pollak, M. Tomkiewicz, *Journal of Physical Chemistry B* 101 (1997) 2730–2734.
- [31] D.G. Barton, M. Shtein, R.D. Wilson, S.L. Soled, E. Iglesia, *Journal of Physical Chemistry B* 103 (1999) 630–640.
- [32] S. Kment, H. Kmentova, P. Kluson, J. Krysa, Z. Hubicka, V. Cirkva, I. Gregora, O. Solcova, L. Jastrabik, *Journal of Colloid and Interface Science* 348 (2010) 198–205.
- [33] A. Fuerte, M.D. Hernández-Alonso, A.J. Maira, A. Martínez-Arias, M. Fernández-García, J.C. Conesa, J. Soria, G. Munuera, *Journal of Catalysis* 212 (2002) 1–9.
- [34] M. Fernández-García, A. Martínez-Arias, A. Fuerte, J.C. Conesa, *Journal of Physical Chemistry B* 109 (2005) 6075–6083.
- [35] G. Li, L. Li, J. Boerio-Goates, B.F. Woodfield, *Journal of the American Chemical Society* 127 (2005) 8659–8666.
- [36] G. Li, J. Boerio-Goates, B.F. Woodfield, L. Li, *Applied Physics Letters* 85 (2004) 2059–2061.
- [37] F.Y.L. Oliva, a.B. Avallé, E. Santos, O.R. Cámara, *Journal of Photochemistry and Photobiology A: Chemistry* 146 (2002) 175–188.
- [38] S. Higashimoto, M. Sakiyama, M. Azuma, *Thin Solid Films* 503 (2006) 201–206.
- [39] M. Aryanpour, R. Hoffmann, F.J. DiSalvo, *Chemistry of Materials* 21 (2009) 1627–1635.
- [40] V.T.T. Ho, C.-J. Pan, J. Rick, W.-N. Su, B.-J. Hwang, *Journal of the American Chemical Society* 133 (2011) 11716–11724.
- [41] M.S. Park, S.K. Kwon, B.I. Min, *Physical Review B* 65 (2002) 161201.
- [42] S. Sharma, B.G. Pollet, *Journal of Power Sources* 208 (2012) 96–119.
- [43] M. Carmo, D.L. Fritz, J. Mergel, D. Stolten, *International Journal of Hydrogen Energy* 38 (2013) 4901–4934.
- [44] A. Damjanovic, V. Brusic, *Electrochimica Acta* 12 (1967) 615–628.
- [45] A. Damjanovic, M.A. Genshaw, *Electrochimica Acta* 15 (1970) 1281–1283.
- [46] S.M. Park, S. Ho, S. Aruliah, M.F. Weber, C.A. Ward, R.D. Venter, S. Srinivasan, *Journal of the Electrochemical Society* 133 (1986) 1641–1649.